Chemical functionalization of the graphene surface for electrical and electrochemical sensing applications

Jiang, L.

Appendix I

Supporting Information for Chapter 2

AI. 1 Materials and methods

GFET device fabrication

To fabricate the GFET devices, the graphene side of the copper growth substrate (CVD graphene, Graphenea S.A.) is glued to a glass slide with a PETMP–TATATO polymer.[1] PETMP–TATATO (Sigma Aldrich) is a clean and biocompatible polymer usually used for dental restorative application.[2] After sufficient photo-initiated crosslinking reaction at room temperature (12 h in daylight), the whole stack (glass-glue-graphene-copper) was oxidized with an O_2 plasma (60 W/0.5 mbar/2 min) to remove the trace of graphene that had grown on the backside of the copper substrate (i.e. the side now facing to the air). To fabricate the source and drain electrodes, both ends of the copper substrate (a strip of copper) were protected by a polymer film of cellulose acetate butyrate (CAB, 30 mg mL^{-1} in ethyl acetate, Sigma Aldrich). An ammonium persulfate solution (0.5 M) was used to etch the non-protected copper foil to reveal the clean CVD graphene supported by the photopolymer and glass substrate without any possible polymer residues. Finally, the fabricated graphene devices were exposed to a hydrogen plasma for different durations to introduce defects with controlled densities.

Thiol–enes polymer

Commercially available pentaerythritol tetra(3-mercaptopropionate) and triallyl-1,3,5-triazine-2,4,6-trione (referred to as PETMP and TATATO, respectively) are used as monomers for the thiol-ene resin formulation. 4:3 volume proportion of PETMP-TATATO were selected for the preparation of the photopolymer.

Plasma condition

A capacitively coupled plasma system with the radio-frequency (RF) of 40 kHz and 200 W power from Diener electronic (Femto) was employed at room temperature. The base pressure of this system is <0.02 mbar. The parameters used for the controlled introduction of defects were 10 W/1.0 mbar for hydrogen plasma and 8 W/0.85 mbar for argon plasma. Specifically, a Faraday cage with grid was employed to shield all the energetic hydrogen ions to form a mild radical plasma to react with graphene.

Characterizations

Raman spectroscopy and mapping were collected from both exfoliated graphene and CVD graphene (using the PMMA transfer method[3]) on SiO_2/Si substrate. Raman spectra on PETMP-TATATO polymer was performed (see Figure AI. 2a). The Raman

spectrometer used is a WITEC alpha300 R – Confocal Raman Imaging with a laser wavelength of 532 nm. To minimize the potential damage from laser heating effect, the laser power was controlled under 1.1 mW. All of the measurements were performed under ambient conditions at room temperature. XPS data were collected from a K-Alpha X-ray photoelectron spectrometer by Thermo Scientific, and the internal reference was adopted with the binding energy of the C 1s peak at 284 eV. Scanning electron microscopy (SEM) images were carried out from a JEOL SEM 6400 microscope. Transmission electron microscopy (TEM) images were collected from a FEI Titan 80–300 microscope. A JPK NanoWizard Ultra Speed AFM was employed to characterize the topology of graphene before and after hydrogenation on SiO_2/Si substrate. The images were scanned in an intermittent contact mode in air at room temperature.

Electrical measurement

The transport measurements of GFET devices upon different hydrogenation times were performed on a SR830 DSP lock-in amplifier with narrow filters. Electrolyte- or electrochemical-gated GFET measurements were carried out in 0.1 M KCl solution containing 10 mM Tris as the buffer (pH 8, both from Sigma Aldrich). The gate voltage was applied on a AgCl/Ag wire as the reference electrode, at a sweep rate at 100 mV s^{-1}, while the source/drain current was fixed at 0.1 μA.

Quantum capacitance

As illustrated in Figure AI. 4, the total capacitance C_{tot} of an electrolyte-gated GFET, is composed of two components in series, quantum capacitance C_q and the electric double-layer capacitance C_{dl}. The C_{dl} for the KCl solution can be approximated as 10–20 μF cm^{-2} for a wide range of ionic concentration >1 mM[4]. C_q is relatively small (~1 μF cm^{-2}) compared to the C_{dl} (in series) and thus dominates the total capacitance $C_q \sim C_{tot}$[5]. By calculating the C_q based on $1/C_{tot} = 1/C_q + 1/C_{dl}$, we get the curves of C_q vs V_{ch} – the potential distributed on graphene channel – derived by $V_{ch} = (V_g C_{dl})/(C_{dl} + C_q)$ for different hydrogenation times.

Electrochemical measurement

The electrochemical experiments were carried out in a homemade one-compartment three-electrode electrochemical cell at ambient conditions. The working electrode is the CVD grown graphene and the counter electrode a platinum wire. All potentials in this work are reported with respect to a saturated Ag/AgCl reference electrode. A potentiostat/galvanostat (CompactStat, Ivium Technologies) was used for the

electrochemical measurements. The electrolyte, 0.1 M KCl, was prepared from KCl (Sigma Aldrich, ≥ 98%) and ultrapure water (Millipore Milli-Q gradient A10 system, 18.2 MΩ.cm). The measured current was normalized to the geometric surface area of the working electrode and not corrected for Ohmic drop as the obtained currents were very low. Prior to the experiments, the cell containing the electrolyte solution was purged with argon to remove the dissolved oxygen.

Table AI. 1 XPS analysis (C 1*s* and O 1*s* peaks) of H- vs Ar-graphene deposited on a Si/SiO_2 wafer

	C 1*s*			O 1*s*		
	BE (eV)		at (%)	BE (eV)		at (%)
H-graphene (fresh)	284	sp^2 C	81.41			
	285	sp^3 C	6.22	532.3	Si-O	86.67
	286	C-O	6.61	533.8	C-O	6.86
	288	C=O	5.76	531.1	C=O	6.47
H-graphene (aged)	284	sp^2 C	79.60			
	285	sp^3 C	8.05	532.4	Si-O	85.79
	286	C-O	5.97	533.6	C-O	6.70
	288	C=O	6.37	531.2	C=O	7.51
Ar-graphene	284	sp^2 C	69.5			
	285.1	sp^3 C	3.01	532.2	Si-O	86.49
	285.8	C-O	12.09	533.5	C-O	6.95
	287.8	C=O	15.41	531.3	C=O	6.57

*aged: one week after sample preparation.

BE: binding energy

AI. 2 Raman characterization of exfoliated and CVD graphene

To better identify the density and the nature of H-sp^3 defects generated through hydrogenation, in this study we conduct Raman mapping on CVD graphene on Si/SiO_2 (Figure AI. 1a) and on exfoliated graphene (Figure AI. 1b). Moreover, Figure AI. 2a shows the Raman spectra acquired on both exfoliated graphene on Si/SiO_2 (left panel)

and CVD graphene on photopolymer (right panel), prepared with minimized contaminations (i.e. no PMMA residues). The signal-to-noise (SNR) ratio is lower in case of CVDG on polymer compared to graphene on Si/SiO_2 because: i) a low laser power is required to prevent heating of the underlying delicate polymer substrate; ii) the redundant peaks from the polymer (at ~1432 cm^{-1} and ~1760 cm^{-1}) render the Raman measurements on CVDG more difficult. Figure AI. 2b shows the peak intensities and the $I(D)/I(G)$ ratio for exfoliated and CVD graphene after 2 s, 5 s and 10 s of hydrogenation. The Raman data for both types of graphene are comparable, suggesting similar quality (i.e. H_2-plasma induced defects) for the two types of graphene.

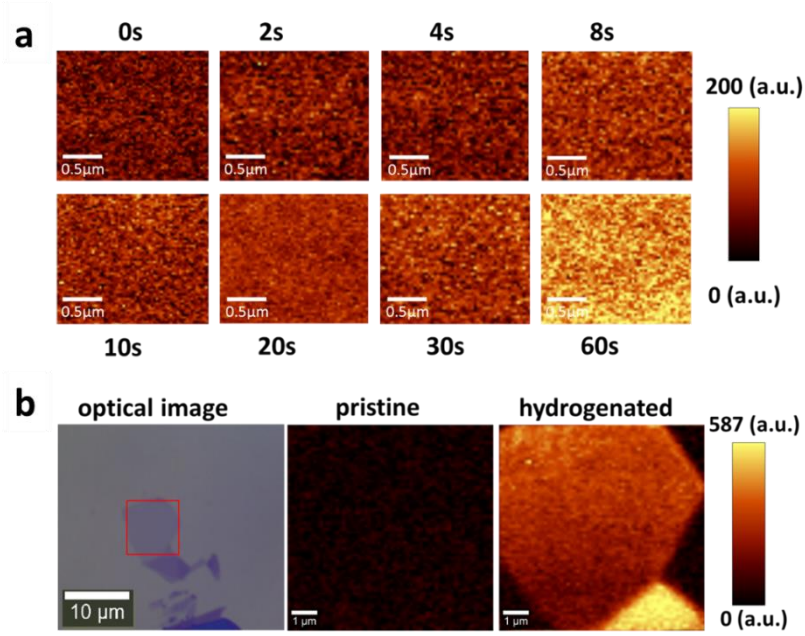

Figure AI. 1 Raman mapping of graphene upon hydrogenation. a) Maps of the D band intensity of CVD graphene with hydrogenation time ranging from 0 to 60 s. b) Maps of the D band intensity for pristine (0 s) and hydrogenated graphene (60 s). Graphene was obtained by exfoliation of natural graphite.

The defect density n_D of H-sp^3 defects in graphene can be estimated based on $I(D)/I(G)$ using Equation 1:[6]

$$n_D = \frac{(1.8 \pm 0.5) \times 10^{22} (I_D/I_G)}{\lambda_L^4} \quad (1)$$

where λ_L denotes the excitation laser wavelength, which is 532 nm here. Moreover, the average distance between defects sites, L_D (nm), can be calculated based on $n_D(\mathrm{cm}^{-2}) = 10^{14}/(\pi L_D^2)$.

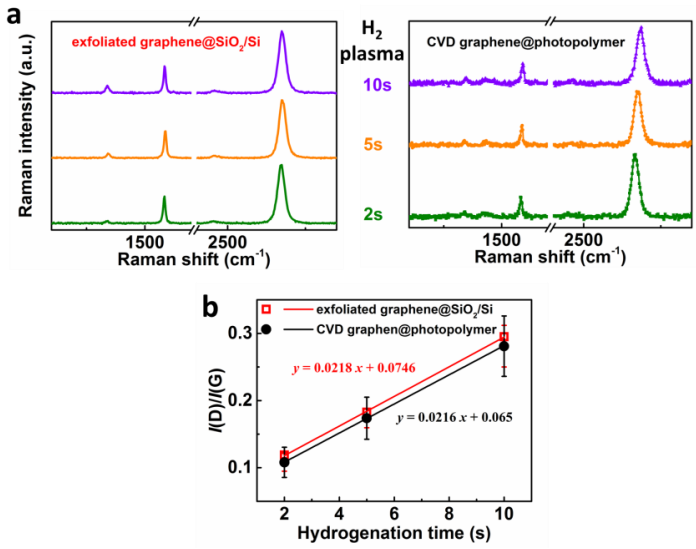

Figure AI. 2 Raman spectra on exfoliated and CVD graphene. a) Raman spectra collected from exfoliated (left panel) and CVD (right panel) graphene after 2 s, 5 s and 10 s of hydrogenation. b) The $I(\mathrm{D})/I(\mathrm{G})$ ratio extracted from exfoliated (red hollow square) and CVD (black solid dot) graphene. The error bars in b) are defined by the standard deviation of experimental values.

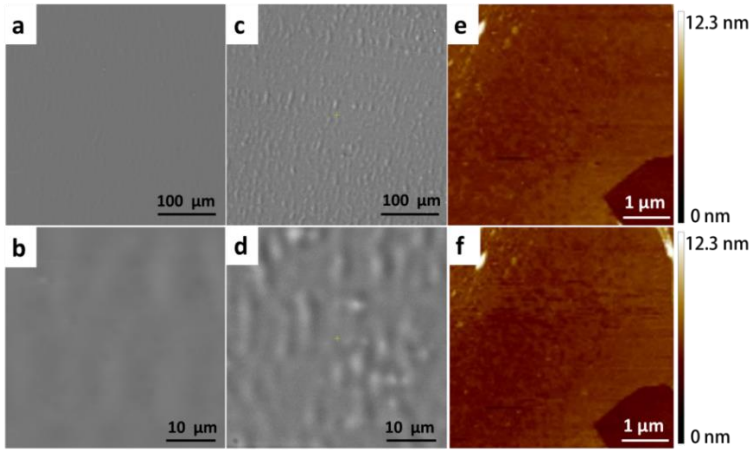

Figure AI. 3 Scanning electron microscopy (SEM) and atomic force microscopy (AFM) of hydrogenated graphene. SEM of hydrogenated graphene on a PETMP-TATATO polymer before (a, b) and after (c, d) hydrogenation. AFM of exfoliated graphene on Si/SiO_2 before (e) and after (f) hydrogenation.

AI. 3 Quantum capacitance calculation

In detail, quantum capacitance (C_q) is measured by adopting a two-electrode configuration (Figure AI. 4). The minimum quantum capacitance, $C_{q,min}$, is related to the additional carrier density n^* by the following Equation 2

$$C_q = \frac{2e^2\sqrt{n_G + n^*}}{\hbar v_F \sqrt{\pi}} \quad (2)$$

where $n_G = (\frac{eV_{ch}}{\hbar v_F \sqrt{\pi}})^2$ represents the carrier density created by the gate voltage (V_g).[7] Then we extracted the n^* from $C_{q,min}$ when $n_G = 0$.

Furthermore, based on self-consistent theory[8], we determine the impurity density, n_{imp}, based on n^*

$$n_{imp} = \frac{n^*}{[2r_s^2 C_0^{RPA}(r_s, a = 4d\sqrt{\pi n^*})]} \quad (3)$$

where $r_s = \frac{2e^2}{\hbar v_F(\epsilon_1 + \epsilon_2)}$, C_0^{RPA} is the correlation function from the random phase approximation (RPA), and d (~1 nm) is the average distance between the charged impurity and graphene. ϵ_1 is the dielectric constant of the photopolymer and ϵ_2 the dielectric constant of electrolyte solution, respectively.

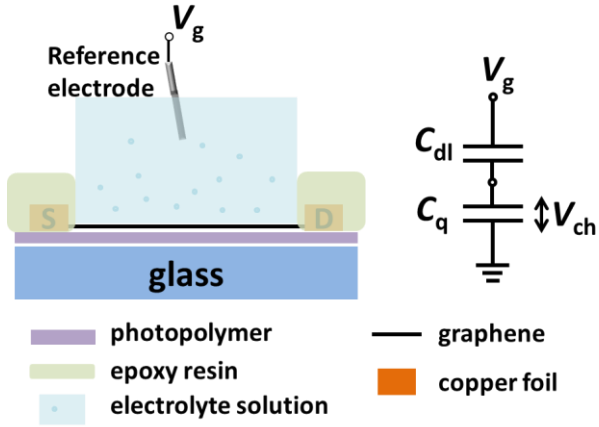

Figure AI. 4 Quantum capacitance measurement setup and circuit illustration.

AI. 4 k^o calculation

We used the Nicholson's method[9] to calculated k^o with Equation 4

$$\psi = k^o(D_O/D_R)^{\alpha/2}(RT/\pi nFD_O\, v)^{1/2} \quad (4)$$

where ψ is a dimensionless kinetic parameter determined by ΔE_p,

$$\psi = \frac{(-0.6288 + 0.00241\, n\, \Delta E_p)}{(1 - 0.017 n \Delta E_p)} \quad (5)$$

α is the transfer coefficient, n is the number of electrons transferred, F is the Faraday constant (96500 C mol^{-1}), D_O and D_R is the diffusion coefficient of redox molecules ($cm^2\ s^{-1}$), v is the scan rate ($V\ s^{-1}$), R is the gas constant ($VCK^{-1}\ mol^{-1}$), and T means the temperature in K. Basically, the diffusion coefficients of the reduced and oxidized form for the redox probe are regarded as approximately equal, which gives α about 0.5. As a result, we can apply the Nicholson's method in a simplified form to determine k^o,

$$\psi = k^o\sqrt{RT/\pi nFDv} \quad (6)$$

Additionally, the diffusion coefficient, D, can be determined by Randles–Sevcik equation

$$i_p = 0.4463\, nFAC\sqrt{\frac{nFDv}{RT}} \quad (7)$$

where A is the effective graphene surfaces that were in contact with electrolyte solution.

AI. 5 Reproducibility

We reproduced the hydrogenation on several CVDG samples which all showed at least around 2-times increase in both the CV current density (Figure AI. 5a) and k^0 (Figure AI. 5b) after 1 s of hydrogenation. The differences between k^0 on untreated graphene can be ascribed to the well-known sample-to-sample variations between CVDG originating from the defects formation during the growth or fabrication, or even airborne contaminations from the environment. In addition, the peak-to-peak separation (ΔE_p) for the redox peaks in Figure AI. 5c has a minimum after 1 s of hydrogenation, indicating a more reversible electrochemical process on H-graphene

(1 s) comparing to untreated graphene and other H-graphene with longer times of hydrogenation treatments.

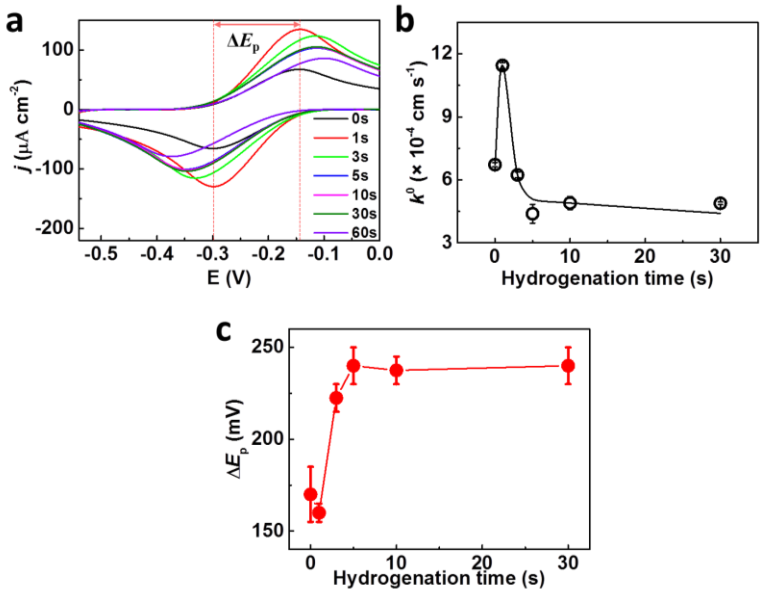

Figure AI. 5 Cyclic voltammograms of hydrogenated graphene. a) Cyclic voltammograms (CVs) collected from the same graphene sample after sequential hydrogenation treatments. The electrolyte solution is 0.1 m KCl containing 10 mM Tris and 1 mM $Ru(NH_3)_6Cl_2$ /$Ru(NH_3)_6Cl_3$, respectively. b) The evolution of electron transfer rate $\boldsymbol{k^0}$, along hydrogenation time, extracted from the cvs plotted in a). c) The peak to peak separation ($\boldsymbol{\Delta E_p}$) vs the hydrogenation time. the error bars in (b-c) are defined by the standard deviation of experimental values.

AI. 6 Averaged total capacitance

In Figure AI. 6, we performed capacitive cyclic voltammetry (CV) in 0.1 M KCl solution containing 10 mM Tris on hydrogenated graphene to understand the impact of hydrogenation on the total capacitance. The capacitive current/current density varies with the scan rate (Figure AI. 6a), and can be unified using Equation 8:

$$i\,(\mathrm{A}) = C(\mathrm{F}) \times v\,(\mathrm{V\,s^{-1}}) \text{ or } j\,(\mathrm{A\,cm^{-2}}) = C(\mathrm{F\,cm^{-2}}) \times v\,(\mathrm{V\,s^{-1}}). \quad (8)$$

We extracted the specific capacitance $C_{\mathrm{ave-tot}}$ of graphene based on the linearity between the current densities and scan rates. For example, the $C_{\mathrm{ave-tot}}$ calculated at the potential of –0.25 V is around 5.37 μF cm^{-2} (Figure AI. 6a and b). Consistent with the trend of k^0 versus hydrogenation, the $C_{\mathrm{ave-tot}}$ (extracted from the CVs in Figure

AI. 6c) also increases dramatically after 1 s, and then decreases (2-10 s) and stabilizes at the level of 7.3 μF cm^{-2} till 30 s.

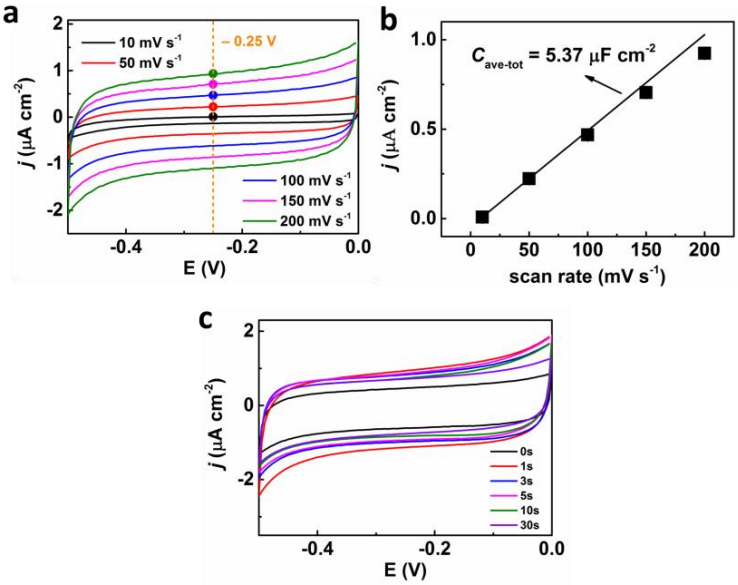

Figure AI. 6 Capacitance measurement for hydrogenated graphene. a) Cyclic voltammograms (CVs) of untreated graphene in 0.1M KCl solution (containing 10 mM Tris) as a function of the scan rate ranging from 10 to 200 mV s^{-1}. b) The plot of the current density (positive-going scan) versus scan rate for an applied potential of –0.25 V. c) Capacitive CVs obtained on graphene before and after 1 to 30 s of hydrogenation. The error bars in (b) are defined by the standard deviation of experimental values.

AI. 7 Raman and electrochemical characterization of Ar treated graphene

To understand to what extend the nature of the defect impacts the electrochemical activity of graphene, we studied vacancy defects on CVD graphene introduced by Ar plasma (Ar-graphene) with comparable defect density levels as for hydrogenated graphene. Figure AI. 7a-b demonstrates the comparable densities (i.e. I(D)/I(G)) of Ar-graphene with hydrogenated ones in Figure 1. The electrochemical measurements on Ar-graphene in Figure 3e and f illustrate the barely varied current density and electron transfer rate under the studied defect density. The result echoes well with previous report[10] where low densities of vacancy defect did not affect the electrochemical activity of the graphene basal plane. However, a dramatically higher density of vacancy defects is expected to improve the electrochemical kinetics at the cost of a lower in-plane electron transport.[11]

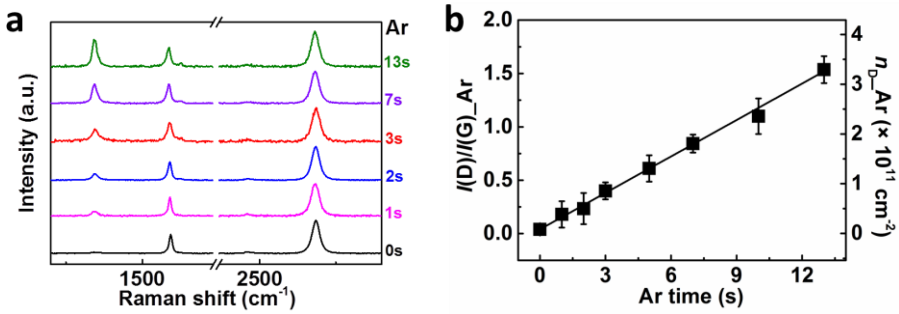

Figure AI. 7 Raman spectroscopy and electrochemistry of Ar-graphene. a) Averaged Raman spectra of CVD graphene transferred on a Si/SiO_2 substrate after the Ar ion plasma (8 w, 0.85 mbar) for 0-13 s. b) The intensity ratio $I(D)/I(G)$_Ar and the derived defect density $\boldsymbol{n}_{\mathbf{D}}$_Ar, plotted vs. the Ar bombarding time. The error bars in (b) are defined by the standard deviation of experimental values.

AI. 8 XPS of H-graphene and Ar-graphene

X-ray photoelectron spectroscopy (XPS) was performed on CVD graphene after hydrogenation and Ar plasma treatment to characterize the chemical stability of plasma treated graphene in ambient condition, and to determine the origin of the H-sp^3 contributions in H-graphene. An asymmetrical fitting function[12] in combination with Gaussian-Lorentzian functions was used to fit the C 1*s* spectra. Other symmetric components were fitted with a Gaussian-Lorentzian fitting function. Shirley background was subtracted for the fitting.

On both fresh and aged (one week) samples (Figure AI. 8a and c), the C 1*s* peak of H-graphene can be deconvoluted into four main peaks: C-C sp^2 (284 eV), C-C sp^3 (285 eV), C-O (286-286.2 eV) and C=O (288 eV).[13] Confirmed by the atomic ratio analysis (in %) in Table AII. 1, the chemical compositions in H-graphene were stable over time, suggesting a negligible oxidation of H-graphene after aging in ambient conditions. The slight decrease in sp^2/sp^3 ratio for aged samples could originate from the further adsorption of airborne hydrocarbon contaminants. Furthermore, the O 1*s* spectra in Figure AI. 8b (fresh) and d (aged) also agree well with 1:1 ratio between single and double bonded oxygen groups in H-graphene, except for the dominant Si-O component (from the Si substrate). Consequently, the detected oxygen bands are likely to be attributed to the residues of polymer (PMMA) employed for the graphene transfer process (PMMA was only used to prepare the XPS samples). In fact, 1) highly ordered pyrolytic graphite (HOPG) was not exposed to PMMA and did not show the O 1*s* band (inset in Figure AI. 8b), and 2) Ar-graphene (Figure AI. 8e and f), which was also exposed to PMMA, showed similar oxygen bands as for H-graphene.

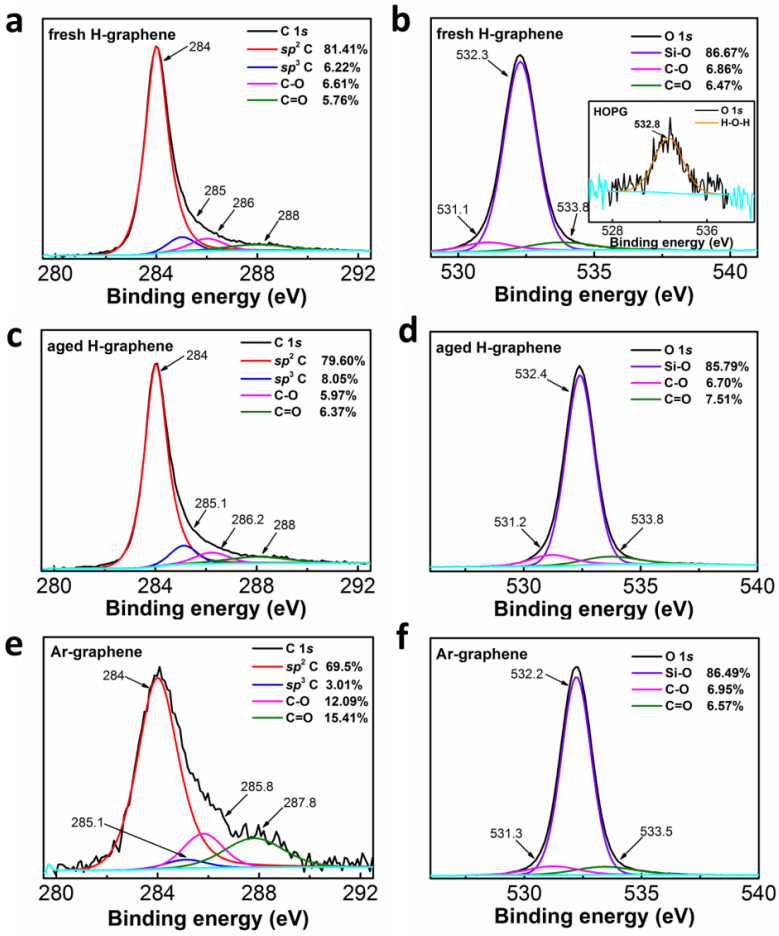

Figure AI. 8 XPS analysis of H-graphene (60 s) and Ar-graphene (13 s) on a Si/SiO_2 substrate. a-b) C 1*s* (a) and O 1*s* (b) spectra of H-graphene in fresh state. Inset in b) is the O 1*s* spectrum for fresh HOPG. c-d) C 1*s* (c) and O 1*s* (d) spectra of H-graphene after aging in atmosphere for one week. e-f) C 1*s* (e) and O 1*s* (f) spectra of Ar-graphene in fresh state.

Furthermore, we compare the C 1*s* peak of graphene containing similar defect densities after 60 s hydrogenation (Figure AI. 8a) and after 15 s of Ar plasma treatment (Figure AI. 8e). In addition to the existence of C–O and C=O components, ~3% sp^3 C component was found in Ar-graphene, which is probably attributed to the surface contaminations (i.e. PMMA residues and hydrocarbons adsorption).

AI. 9 References

[1] W. Fu, C. Nef, A. Tarasov, M. Wipf, R. Stoop, O. Knopfmacher, M. Weiss, M. Calame, C. Schönenberger, *Nanoscale* **2013**, 5, 12104.

[2] N. B. Cramer, C. L. Couch, K. M. Schreck, J. A. Carioscia, J. E. Boulden, J. W. Stansbury, C. N. Bowman, *Dent. Mater.* **2010**, 26, 21.

[3] X. Liang, B. A. Sperling, I. Calizo, G. Cheng, C. A. Hacker, Q. Zhang, Y. Obeng, K. Yan, H. Peng, Q. Li, X. Zhu, H. Yuan, A. R. Hight Walker, Z. Liu, L.-m. Peng, C. A. Richter, *ACS Nano* **2011**, 5, 9144.

[4] S. Baldelli, *Acc. Chem. Res.* **2008**, 41, 421.

[5] J. Xia, F. Chen, J. Li, N. Tao, *Nature Nanotechnology* **2009**, 4, 505.

[6] L. G. Cançado, A. Jorio, E. M. Ferreira, F. Stavale, C. Achete, R. Capaz, M. Moutinho, A. Lombardo, T. Kulmala, A. Ferrari, *Nano Lett.* **2011**, 11, 3190.

[7] A. Das, S. Pisana, B. Chakraborty, S. Piscanec, S. Saha, U. Waghmare, K. Novoselov, H. Krishnamurthy, A. Geim, A. Ferrari, *Nat. Nanotechnol.* **2008**, 3, 210.

[8] S. Adam, E. Hwang, V. Galitski, S. D. Sarma, *Proc. Natl. Acad. Sci.* **2007**, 104, 18392.

[9] R. S. Nicholson, *Anal. Chem.* **1965**, 37, 1351.

[10] a) M. Velický, M. A. Bissett, P. S. Toth, H. V. Patten, S. D. Worrall, A. N. Rodgers, E. W. Hill, I. A. Kinloch, K. S. Novoselov, T. Georgiou, *Phys. Chem. Chem. Phys.* **2015**, 17, 17844; b) J.-H. Zhong, J. Zhang, X. Jin, J.-Y. Liu, Q. Li, M.-H. Li, W. Cai, D.-Y. Wu, D. Zhan, B. Ren, *J. Am. Chem. Soc.* **2014**, 136, 16609.

[11] L. Vicarelli, S. J. Heerema, C. Dekker, H. W. Zandbergen, *ACS Nano* **2015**, 9, 3428.

[12] G. Wertheim, *J. Electron Spectrosc. Relat. Phenom.* **1975**, 6, 239.

[13] A. Ganguly, S. Sharma, P. Papakonstantinou, J. Hamilton, *J. Phys. Chem. C* **2011**, 115, 17009.

Appendix II

Supporting Information for Chapter 3

AII. 1 Materials and methods

Materials

Chemical vapor deposition (CVD) graphene is grown on a polycrystalline copper foil (Alfa Aesar, 99.999% purity, 25 mm thickness) in a commercially available hot-wall chamber (planarGROW-2B, planarTECH). Epoxy resin (including the curing agent) was supplied by GENTEC. Poly(methyl methacrylate) (Sigma Aldrich) was used for CVD graphene transfer. Cellulose acetate butyrate (CAB, ~30 mg/mL in ethyl acetate), potassium chloride (KCl, ≥99.0%), potassium ferricyanide ($K_3Fe(CN)_6$, ≥99.0%) and ammonia persulfate ($(NH_4)_2S_2O_8$, ≥98.0%) were supplied by Sigma Aldrich. Sulfuric acid (98% H_2SO_4, ≥99.999%) and sodium hydroxide monohydrate ($NaOH{\cdot}H_2O$, TraceSelect ≥99.9995%) were purchased from Honeywell Fluka. Potassium perchlorate ($NaClO_4$, EMSURE®) was ordered from Merck. The electrolyte solution was prepared with ultrapure water (Millipore Milli-Q gradient A10 system, 18.2 MΩ.cm). All gas were supplied by Linde Gas (5.0).

Plasma condition

A capacitively coupled plasma system with a radio-frequency (RF) of 40 kHz and 200 W power from Diener electronic was employed at room temperature. The base pressure of this system is less than 0.02 mbar. To achieve mild plasma conditions, a Faraday cage equipped with grid was employed to shield all the energetic ions, thus forming a mild radical plasma to treat the graphene samples inside the cage. The parameters used for nitrogenation treatments were 16 W power and 0.8 mbar pressure for ammonia plasma. Oxygen plasma was applied with a power of 30W and a pressure of 0.5 mbar.

Structure characterization

Raman spectra and mapping were collected using a WITEC alpha300 R – Confocal Raman Imaging with a laser wavelength of 532 nm. A 100× magnification objective was used to form a laser inspection region of 300 μm in diameter. To minimize the potential damage from laser heating effect, the laser power was controlled under 2 mW. All of the measurements were performed under ambient conditions at room temperature.

The electric transport measurements of graphene field-effect transistor devices were performed on a SR830 DSP lock-in amplifier with narrow filters. Electrolyte- or electrochemical-gated GFET measurements were carried out in 0.1 M KCl solution containing 10 mM Tris as the buffer (pH 8). The gate voltage was applied on a AgCl/Ag

wire as the reference electrode, at a sweep rate of 100 mV s^{-1}, while the source/drain current was fixed at 0.1 μA.

XPS were performed using a K-Alpha X-ray photoelectron spectrometer equipped with a monochromatic X-ray source (Al Kα = 1486.6 eV) by Thermo Scientific. Energy calibration was performed by refereeing to the C 1s peak of highly ordered pyrolytic graphite (HOPG) at 284.6 eV and CasaXPS software was used to analyze the spectra fitting.

Electrochemical measurements

The electrochemical experiments were carried out in a custom made one-compartment three-electrode electrochemical cell at ambient conditions. The working electrode is the as-prepared graphene and the counter electrode a graphite rod. All potentials in this work are reported with respect to a reversible hydrogen electrode (RHE) reference electrode, a Pt mesh in H_2 saturated electrolyte operating at the same pH and connected to cell via a Luggin capillary. Autolab PGSTAT 12 potentiostats operated by NOVA software were used for the electrochemical measurements. The measured current was normalized to the geometric surface area of the working electrode and not corrected for ohmic drop as the obtained currents were very low. Prior to the ORR experiments, the cell containing the electrolyte solution was purged and saturated with O_2. For capacitive current measurements, argon was purged at least for 30 min to fully remove dissolved O_2 in the solution. The cyclic voltammetry and polarization curves were measured at a scan rate of 100 mV s^{-1}.

Pure graphene on epoxy support

Epoxy resin (100:45 mass ratio of base to curing agent, EPO-TEK) was slowly poured onto a glass slide substrate (thus air bubble in the mixture was avoided) after homogeneous mixing and degassing in vacuum for 45 min to form a thin layer. The top side of the as-grown CVD graphene on copper foil (~1.5 mm × 10 mm) was glued attached to the epoxy resin layer (homogeneously mixed with the curing agent) sitting on a glass slide. After the epoxy resin was cured at room temperature for 24 hours, the attached graphene was isolated from the air by the coverage of the air-tight epoxy and the growth copper substrate. Next, graphene that had grown in the backside of the copper (now facing to the air) was removed using an oxygen plasma (100 W/0.5 mbar/2 min). After protecting the copper end with a clean and hydrophobic film of cellulose acetate butyrate (CAB), ammonia persulfate solution (0.5 M) was used to etch the non-protected copper and to expose the underlying graphene, referred to as pure graphene. Then the graphene was wired out (using silver epoxy) via the retained

copper foil with a low contact resistance. For the fabrication of graphene field effect transistor devices, similar procedures were adopted except that two ends of the copper foil (a strip of copper) were preserved as source and drain electrodes, respectively.

RRDE preparation

The glassy carbon (GC) disk electrode (0.196 cm2) and platinum ring were supplied by Pine Instruments, and controlled by a Pine MSR rotator in a ChangeDisk configuration. Prior to use, both the disk and ring electrodes were mechanically and separately polished with 1.0, 0.3 and 0.05 micron alumina slurry respectively for 2 min with subsequent rinsing and sonication in water for 10 min. The separate polishing of ring and disk excluded any potential contamination of platinum onto the GC disk electrode. After polishing and cleaning, poly(methyl methacrylate) (PMMA) was spin-coated onto the CVD graphene on copper foil and cured to form a carrier film. After the underlying copper was etched in ammonium persulfate solution, PMMA-graphene layer floating on water (to rinse ammonium salt out) was transferred onto the target substrate, i.e. the GC disk (proposed as monolayer graphene on RRDE) or CVD graphene on copper foil (for bilayer graphene preparation). Finally the transferred graphene was obtained by removing PMMA in acetone. Electrochemical RRDE experiments were carried out in a two-compartment cell with a three-electrode set-up. The counter electrode was separated from the rotating disk electrode via a water permeable glass frit in a different compartment. A capacitor of 10 μF was connected between the RHE and electrolyte solution through a platinum wire to lower the noise ratio especially for the ring current.

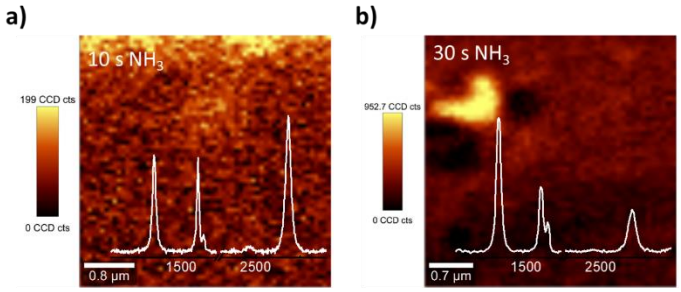

Figure AII. 1 Raman spectroscopy of nitrogenated graphene. Raman mapping of D band intensity of nitrogenated graphene after 10 s (a) and 30 s (b) of nitrogenation treatments, respectively. The insets are the corresponding Raman spectra.

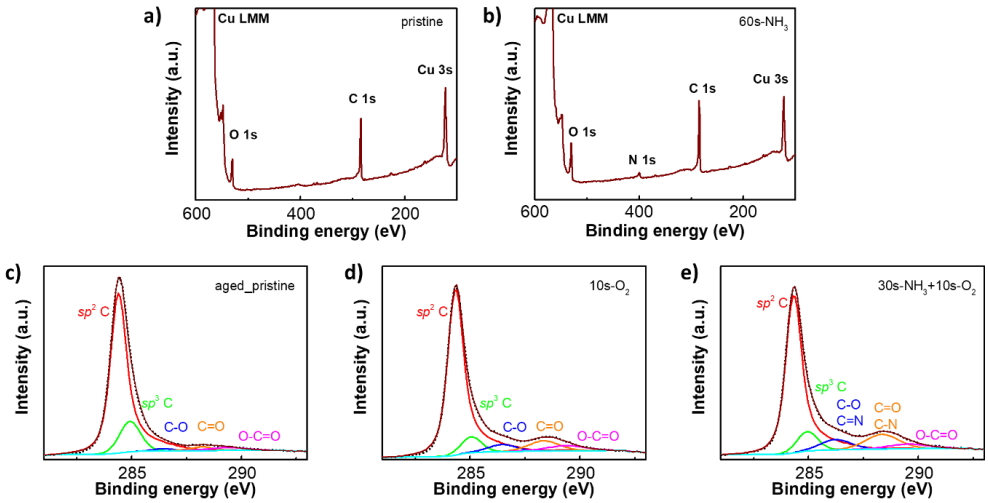

Figure AII. 2 XPS analysis for graphene on copper. a) Survey spectrum for pristine graphene. b) Survey spectrum for graphene treated with 60 s of nitrogenation. c) C1*s* core spectra for aged (1 month) pristine graphene. d) C1*s* core spectra for graphene upon 10 s of oxidation. e) C1*s* core spectra for graphene co-doped with 30 s of nitrogenation and 10 s of oxidation.

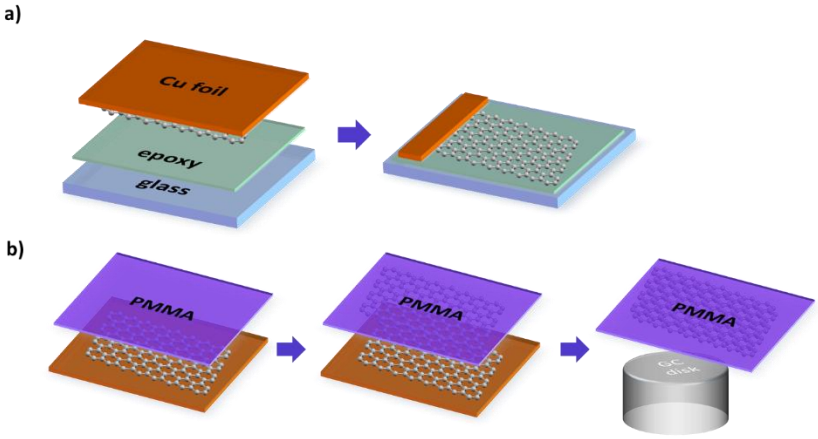

Figure AII. 3 Illustration schemes of graphene surface preparations for ORR measurements. a) Preparation of pure graphene surface supported on epoxy resin. b) Bilayer graphene surface (referred to as RRDE graphene), the opposite face of the pure graphene in (a), is transferred on the glassy carbon (GC) disk.

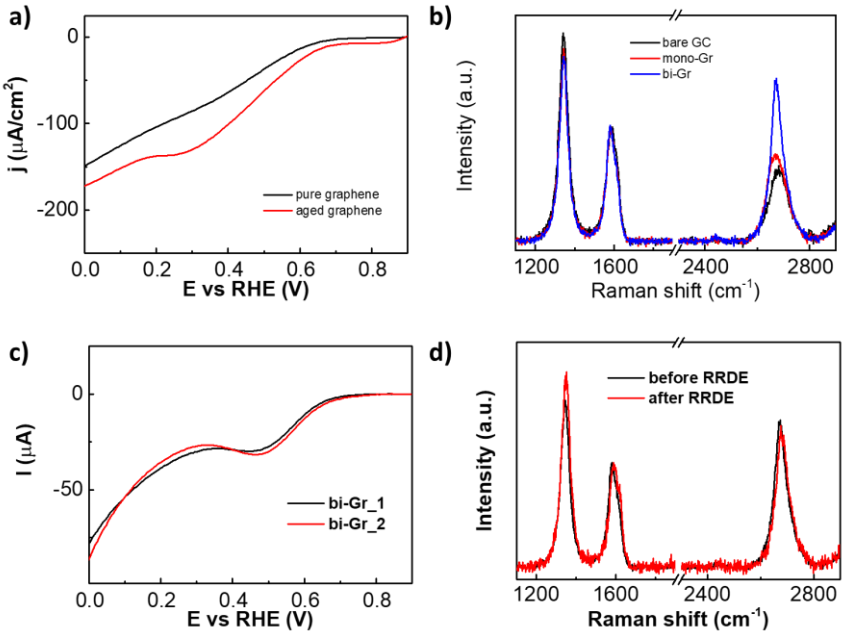

Figure AII. 4 ORR activity and Raman spectroscopy of graphene. a) LSV curves of an aged graphene sample on epoxy substrate with an evident peak at ~0.4 V as compared to pure graphene. b) Raman spectra of bare GC, monolayer and bilayer graphene supported by GC. c) LSV polarization curves of two samples of bilayer graphene (denoted as bi-Gr) supported by the same GC disk electrode at 800 rpm in 0.1 M sodium hydroxide solution saturated with O_2. d) Raman spectra of the bilayer graphene on the GC disk before and after RRDE experiment.

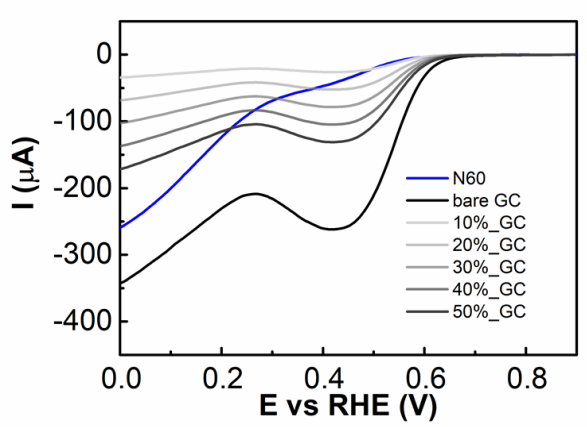

Figure AII. 5 Comparison of the ORR activity of N60 graphene on RRDE versus the GC disk. LSV curves for 60 s nitrogenated graphene on the GC disk (N60) and for the GC disk with full (bare GC) or partial exposure (10% to 50%) in terms of the electrode area. The electrolyte solution is 0.1 M sodium hydroxide saturated with O_2.

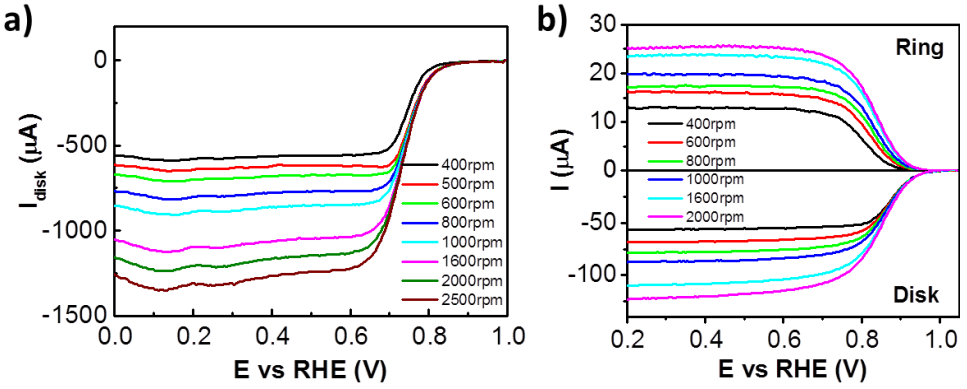

Figure AII. 6 Levich constant and collection efficiency. a) ORR polarization curves at different rotation rates on a platinum disk electrode in 0.1 M NaOH solution saturated with O_2. b) Currents on the GC disk and platinum ring electrodes for 1 mM $K_3Fe(CN)_6$ in 0.1 M $NaClO_4$ purged with argon at different rotation speeds.

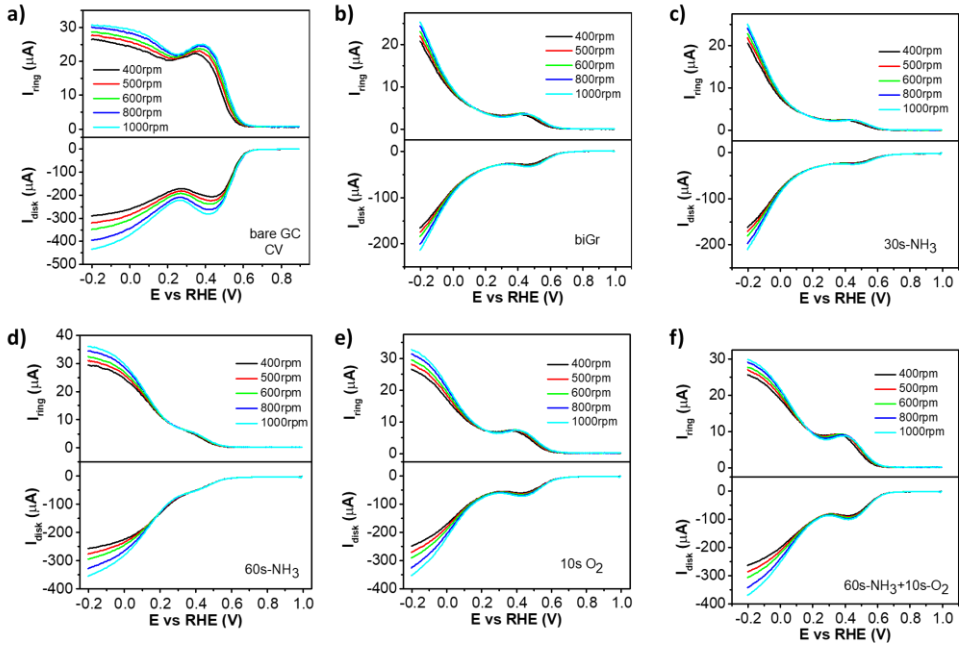

Figure AII. 7 ORR polarization curves of graphene at different rotation rates for Koutecky-Levich plots. a) Bare GC electrode. b) Bilayer graphene on GC electrode. c) 30s nitrogenated graphene. d) 60 s nitrogenated graphene. e) 10s oxygenated graphene. f) 60s nitrogenated and 10 s oxygenated graphene.

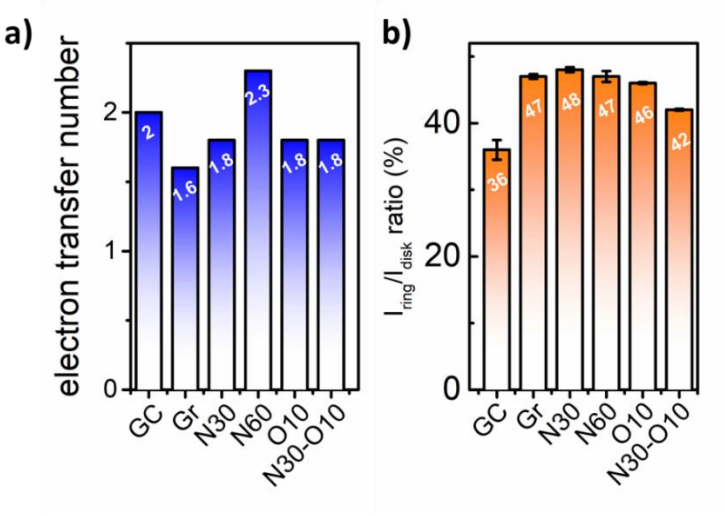

Figure AII. 8 The ORR selectivity of the GC disk and RRDE graphene. a) Electron transfer number based on the K-L plots. b) The ratios of I_{ring} over I_{disk}.

Table AII. 1 Defect density (n_D) and interdefect distance (L_D) analysis based on nitrogenation time

NH_3 time (s)	0	2	4	6	8
n_D ($\times 10^{10}$ cm^{-2})	1±0.1	3.1±0.4	10.2±0.9	17.6±1.5	21.6±3.2
L_D (nm)	~56.6	~32.0	~17.7	~13.5	~12.2
NH_3 time (s)	10	20	30	60	
n_D ($\times 10^{10}$ cm^{-2})	23.2±1.2	3.9±1.5	4.8±2.9	5.5±1.4	
L_D (nm)	~11.7	~9.0	~8.1	~7.6	

AII. 2 Electrical doping effect in N-doped graphene

It is known that the incorporation of N atoms into the two-dimensional in-plane of graphene can vary in different configurations of pyridinic, quaternary and pyrrolic N, that exert distinct effects on the electronic structures and transport properties of graphene.[1] Normally pyridinic and pyrrolic N p-dopes graphene while quaternary N introduces n-type doping in graphene. Of note, a weak n-doping effect can be found in hydrogenated pyridinic and pyrrolic N wherein the extra charge on N is forced into the delocalized carbon π-network.[2] Quaternary N sites have been reported to act as a positively charged scattering center, which can enhance the electron-hole asymmetry in transport properties.[3] Given the observed n-doping behavior as well as the symmetric G (V_g) curves, it is expected that hydrogenated pyridinic and/or pyrrolic N are the dominant configurations in the N-doped graphene of this study.

AII. 3 Working principle of graphene field effect transistor (GFET)

Using AgCl/Ag as the reference electrode, the gate voltage (V_g) is applied through the electrolyte solution (0.1 M KCl with 10 mM Tris, pH ~8). When V_g sweeps from negative to positive voltages, the dominant charge carriers in graphene correspondingly change from hole to electron as the Fermi level (E_F) of graphene shifts from the valence band to the conduction band. As a result, the conductance (G) of graphene demonstrate an ambipolar behavior with V_g in Figure 1c (black line). The voltage of the minimum conductance (G_{min}) is called charge neutrality point (CNP) with equal concentrations of hole and electron carriers. The positive CNP (80 mV) for untreated graphene suggests a positive doping from the underneath epoxy substrate.

AII. 4 Reproducibility and reliability of the bilayer graphene on the GC disk

Raman spectroscopy and repeated ORR tests were performed to confirm the reliability and reproducibility of the bilayer graphene on the GC disk (RRDE graphene). The Raman spectra of monolayer and bilayer graphene on the GC electrode both show increased peak intensity of 2D peak compared to that of the bare GC (Figure AII. 4b). Especially the peak intensity ratio of I(2D)/I(G), an indicator of graphene layer number,[4] is as high as 1.4 for bilayer graphene while below 1.0 for both monolayer graphene (0.75) and the GC (0.65). Therefore, we can conclude that bilayer graphene behaves more independently than monolayer graphene supported on GC. In addition, the well-overlapped LSV curves at 800 rpm obtained from two different bilayer graphene samples in Figure AII. 4c show a good reproducibility. Raman characterization of bilayer graphene before and after RRDE experiments (Figure AII. 4d) confirms the stability of bilayer graphene. As a result, bilayer graphene is used as a pristine surface on RRDE for further doping treatments and ORR catalysis.

AII. 5 Selectivity of RRDE graphene

1) Koutecky-Levich equation

At different rotation rates, the limiting current for oxygen reduction behaves according to the Koutecky-Levich equation[5]:

$$\frac{1}{I} = \frac{1}{I_{\mathrm{K}}} + \frac{1}{I_{\mathrm{L}}} \qquad (1)$$

where I is the observed current, I_{K} is the kinetic current that can be observed when the mass transport rate to the electrode is much greater than the reaction rate, I_{L} is the diffusion limited current that can be obtained when the reaction rates is much larger than the mass transport rate. The diffusion-limited current can be described by the Levich equation:

$$I_{\mathrm{L}} = 0.62nFAD_O^{2/3}C_O v^{-1/6}\omega^{1/2} = BnA\omega^{1/2} \qquad (2)$$

where n is the electron transfer number, F is the Faraday constant (C mol^{-1}), A is the electrode area (cm^2), D_{O} is the diffusion coefficient of O_2 (cm^2 s^{-1}), C_{O} is the concentration of O_2 in the electrolyte, v is the kinematic viscosity (cm^2 s^{-1}) and ω the rotation rate (rad s^{-1}). The equation can be simplified with the Levich constant defined as B. By performing rotating ring disk electrode (RRDE) experiments for ORR with a platinum disk electrode (Figure AII. 6a), B can be calculated using the slope of the

Koutecky-Levich plot (as platinum is known to be a 4-electron dioxygen reduction catalyst):

$$slope = \frac{1}{BnA} \quad (3)$$

The Koutecky-Levich plots in Figure 4f compares the activities for different RRDE graphene using the intersection at the axis of $1/I_{\text{disk}}$, which corresponds to the kinetics current (I_{K}). A higher I_{K}, a direct indicator of a higher catalytic activity, will be reflected by a value of the $1/I_{\text{disk}}$ intersection closer to zero. As expected, the co-doped sample N30-O10 shows the best ORR activity by intersecting with the $1/I_{\text{disk}}$ axis the closest to zero, while the low current values are found at the pristine and N30 samples as their $1/I_{\text{disk}}$ intersections are the furthest from zero.

2) Collection efficiency

The collection efficiency of rotating disk ring electrode (RRDE) was calculated based on the reversible redox reaction of potassium ferricyanide. In 0.1 M sodium perchlorate purged with argon, 1 mM potassium ferricyanide (III) was reduced at the glassy carbon disk to Fe(II) which can be re-oxidized at the platinum ring. Of note, the reversible hydrogen electrode (RHE) as the reference electrode in the Luggin capillary was only in contact with 0.1 M sodium perchlorate. As illustrated in Figure AII. 6b, the redox currents were recorded at both the disk and ring at different rotation rates ranging from 400 to 2000 rpm. Based on the currents, the collection efficiency ratio of the ring was determined as 22.5%.

AII. 6 References:

[1] Y.-F. Lu, S.-T. Lo, J.-C. Lin, W. Zhang, J.-Y. Lu, F.-H. Liu, C.-M. Tseng, Y.-H. Lee, C.-T. Liang, L.-J. Li, *ACS Nano* **2013**, 7, 6522.

[2] a) Z. Jin, J. Yao, C. Kittrell, J. M. Tour, *ACS Nano* **2011**, 5, 4112; b) T. Schiros, D. Nordlund, L. Pálová, D. Prezzi, L. Zhao, K. S. Kim, U. Wurstbauer, C. Gutiérrez, D. Delongchamp, C. Jaye, *Nano Lett.* **2012**, 12, 4025.

[3] J. Li, L. Lin, D. Rui, Q. Li, J. Zhang, N. Kang, Y. Zhang, H. Peng, Z. Liu, H. Xu, *ACS Nano* **2017**, 11, 4641.

[4] Y. Hao, Y. Wang, L. Wang, Z. Ni, Z. Wang, R. Wang, C. K. Koo, Z. Shen, J. T. Thong, *Small* **2010**, 6, 195.

[5] A. J. Bard, L. R. Faulkner, J. Leddy, C. G. Zoski, *Electrochemical methods: fundamentals and applications*, wiley New York, **1980**.

Appendix III

Supporting Information for Chapter 4

AIII. 1 Materials and Methods

Plasma condition

A capacitively coupled plasma system with a radio-frequency (RF) of 40 kHz and a base pressure below 0.02 mbar (Diener electronic, Femto) was employed at room temperature. The power/pressure parameters used for controlled surface modifications were 10 W/1.0 mbar for hydrogen plasma and 8 W/0.85 mbar for argon plasma, respectively. Inside the plasma chamber, a perforated Faraday cage was used to shield energetic hydrogen ions to form a mild radical plasma to react with graphene.

(HR)TEM characterization

CVD graphene (Graphenea) was employed to prepare the samples. We deliberately opted for commercial graphene to assure reproducibility. Aberration-corrected high-resolution transmission electron microscopy (AC-HRTEM) imaging was conducted on an FEI Titan 80–300 microscope at an acceleration voltage of 80 kV (Ulm University). Transmission electron microscopy (TEM) images were collected on a Tecnai F20 microscope (Thermo-Fisher Scientific) operating at 200 keV (Leiden University Medical Center, LUMC).

TPD-IR characterization

The temperature programmed deposition-infrared spectroscopy (TPD-IR) was performed in a custom-made high vacuum system, comprising a central high vacuum chamber with a closed-cycle helium refrigerator mounted on top. Water deposition on a BaF_2 window mounted on the tip of a cold finger can be monitored using a Fourier Transform Infrared (FTIR) spectrometer. IR spectra in the range of 700-4000 cm^{-1} and with a resolution of 1 cm^{-1} were collected in transmission mode at normal incidence every 90 seconds. CVD graphene films were transferred onto the BaF_2 window via a biphasic method previously developed.[1]

Near-ambient pressure (NAP)-XPS experiments

NAP-XPS spectra were recorded with a SPECS XPS spectrometer equipped with a monochromatic small-spot (300 μm) X-ray source, an Al anode (Al Kα= 1486.6 eV) and a 180° double-focusing hemispherical analyzer working with a multichannel 1D delay-line detector. XPS measurements at pressures of up to 20 mbar are possible due to a differential pumping system, which separates the electron analyzer (SPECS Phoibos NAP-150) from the reaction area via a nozzle with an aperture of 300 μm.

Filling of the NAP-cell with water vapor was performed by means of piezo-electric leak valve. The water reservoir was kept at room temperature. Further details about the design of the NAP-XPS cell can be found in literature.[2] UHV measurements were conducted at a chamber pressure of $<10^{-9}$ mbar. XP spectra were processed by CasaXPS software using Shirley background subtraction.

Raman spectroscopy

Raman spectra were collected on a WITEC alpha300 R – Confocal Raman Imaging with a laser wavelength of 532 nm. Laser power was set to <2 mW to minimize potential damages from laser induced heating of the samples. All measurements were performed under ambient conditions at room temperature.

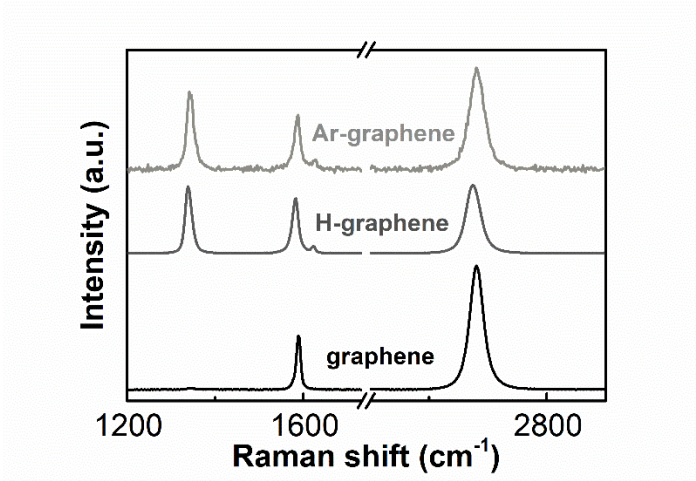

Figure AIII. 1 Raman spectra of graphene, H-graphene and Ar-graphene. Similar densities of hydrogenated and vacancy defects are confirmed by the peak intensity ratio between D (~1350 cm^{-1}) and G peaks (~1580 cm^{-1}). The spectra recorded using a 2.33 eV (532 nm) laser excitation are calibrated according to the G peak intensity.

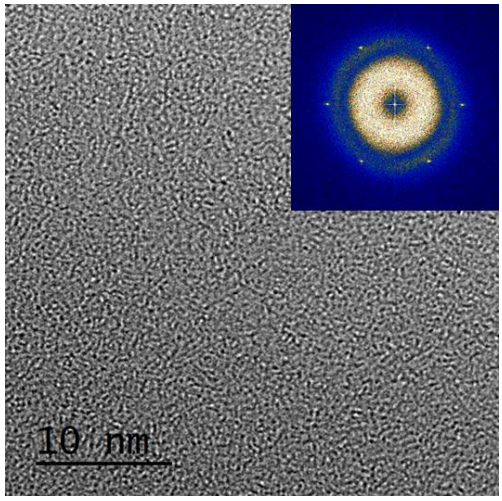

Figure AIII. 2 HRTEM images of pristine graphene. The amorphous patterns caused by the surface-adsorbed hydrocarbons cover all over the graphene lattice within the image views. The inset FET patterns of six reflections 4.7 nm^{-1} in a) suggest the good crystallinity of pristine graphene.

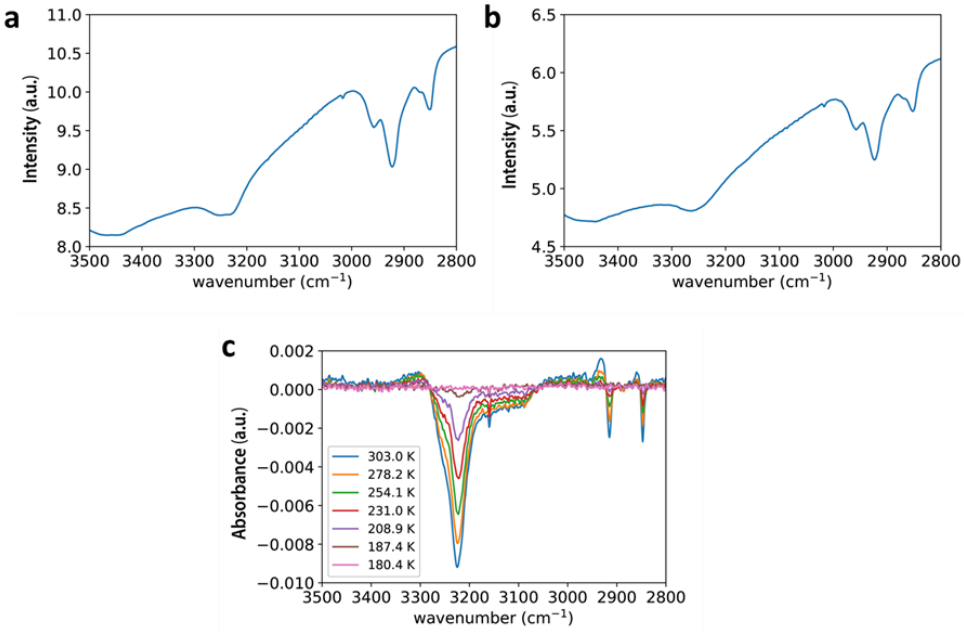

Figure AIII. 3 TPD-IR tests of water adsorption. a) Background spectra for pristine graphene. b) Background spectra for 60 s hydrogenated graphene. c) IR spectra during cooling down from room temperature to 180 K. The peak around 3250 cm^{-1} indicates water desorbed from H-graphene surfaces.

Table AIII. 1 Process flow for analyzing the images

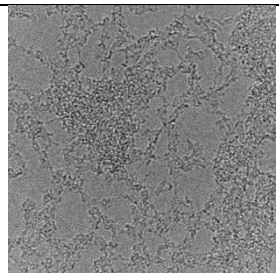	**Step 1: Conversion into a grayscale image** The TEM image is converted into a grayscale image using the MATLAB built-in function rgb2gray().
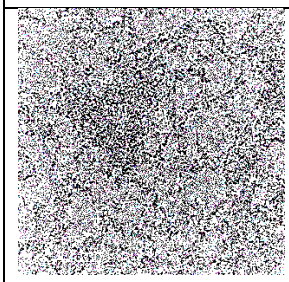	**Step 2: Adjusting of the contrast** The goal of this step is to increase the contrast of the image and improve the visibility of small contaminations. Built-in adapthisteq() function of the MATLAB performs this task by contrast-limited adaptive histogram equalization.
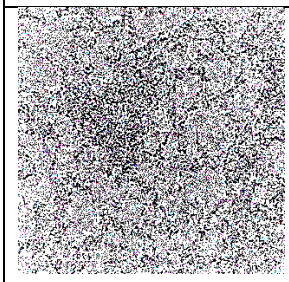	**Step 3: Normalization of the image** The goal of this step is to eliminate the effect of any intensity variations from image to image. The intensity of each pixel of the image after this transformation (y) is calculated by: $y = 255 \times \frac{(x-min)}{(max-min)}$, where: x: the gray scale initial intensity of the pixel min: minimum gray scale intensity for the original image. max: maximum gray scale intensity for the original image.
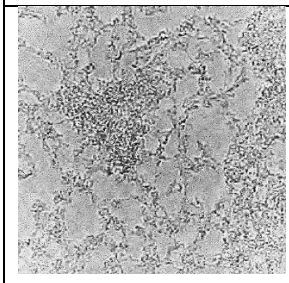	**Step 4: Denoising of the image** Several MATLAB built-in functions including imopen(), imclose(), imgaussfilt() are used to remove the noise. Opening and closing operations remove random flipped pixels. The imgaussfilt() smoothens the image by filtering with a 2-D Gaussian function.

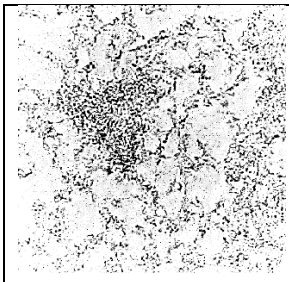	**Step 4: Conversion the *gray-scale* into the *binary* image** With this conversion, all the pixels with the intensity greater than a threshold, calculated by the adaptthresh() function will be replaced by 1 (white color, corresponding to the clean graphene) and the pixels with lower intensities will be replaced by 0 (black, corresponding to contaminations). This operation is performed using the MATLAB built-in function imbinarize().
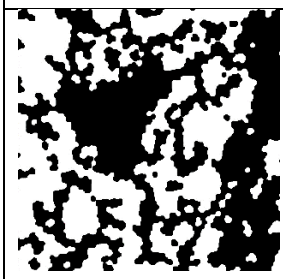	**Step 5: Segmentation** By using the built-in open()/close() functions (subsequent erosion and dilation operations) the extend of the contaminations is identified. A disk with the radius of 10 pixels is used as the structuring element to define the neighborhood. The cleanness of the image is eventually calculated as the sum of the number of the white pixels (clean graphene area) normalized by the total number of pixels.

AIII. 2 MATLAB script to calculate the cleanness

```
%% Initialization

N = 50; % number of the images to be analyzed.
level= 0.50; % bw conversion treshold value.
size = 10;

report = zeros (N , 3);
shape = 'disk';

for sequence = 1: N
 filename = num2str(sequence);
 im = imread([filename, '.tif']);

 image = rgb2gray(im); %rgb to gray conversion

 IniImage = image;

 %% improving the image

 image = adapthisteq(image); % increasing the image contrast

 image = uint8(255*mat2gray(image)); % normalization of the image
```

```
%% Noise removal

image = imclose(image,strel(shape,1));
image = imopen(image,strel(shape,1));

image = imgaussfilt(image, 2);

%% conversion to a binary mage

T = adaptthresh(image,level,'ForegroundPolarity','dark');
image = imbinarize(image, T);


%% segmentation

image = imopen(image, strel(shape,size));
image = imclose(image, strel(shape,size));

%% finalizing
clean = sum(sum(image == 1));
total = numel(image);

report(sequence, 1) = clean;
report(sequence, 2) = total;
report(sequence, 3) = clean*100/total;

figure, imshowpair(IniImage, image, 'montage'), title([filename, ': cleanless:', num2str(report(sequence, 3)), '%,', ', size:', num2str(size), ', level: ', num2str(level)]);
saveas(gcf,[filename, '_3rd_analyzed.jpg']);

clear image
clear im
clear IniImage
clear Image
end

figure, bar(report(:, 3));
figure, hist(report(:, 3));
Clenaliness = mode(report(:, 3));
display(Clenaliness);
```

AIII. 3 References

[1] L. A. Belyaeva, W. Fu, H. Arjmandi-Tash, G. g. F. Schneider, *ACS Cent. Sci.* **2016**, 2, 904.

[2] L. Nguyen, F. Tao, *Rev. Sci. Instrum.* **2016**, 87, 064101.

Appendix IV

Supporting Information for Chapter 5

AIV. 1 Materials and methods

Preparation of graphene samples

Graphene was grown in a CVD oven (nanoCVD system, Moorfield Nanotechnology, England). Briefly, the copper foil (Alfa Aesar, 99.999% purity, 25 μm thickness) was rapidly (in ~ three minutes) heated to 1035°C in the chamber and annealed under the continuous flow of hydrogen (20 standard cubic centimeters per minute, sccm) for 90 minutes. Graphene grow started upon the injection of methane (CH_4:H_2 ratio of 2:20) for 2 minutes; then the hot stage assembly cooled down under Ar environment. The size of the hot-stage of our CVD chamber allows the growth of the samples as large as 2.5 cm × 4 cm; graphene on the backside of the copper foil was etched away upon the exposure to oxygen plasma while the front side was protected with a piece of aluminium foil, sealed at the edges with scotch tapes. Use of PMMA was avoided as PMMA left-over might increase the uncertainties in estimating the mechanical properties of graphene. The absence of the D peak in Raman spectroscopy of the front side of the randomly tested samples at this stage, confirmed the quality of the sealing. Graphene on copper sample was sectioned using a sharp blade into pieces of ~1 cm × 1 cm to be used separately at different compression experiments.

Manipulating the lattice of graphene

Argon ion irradiation and hydrogenation of the graphene lattice were performed in a capacitively coupled RF plasma system operating at 40 kHz and 200 W power from Diener electronic. The base pressure of this system is below 0.02 mbar. Thorough flushing (3 to 5 times) of the chamber with the corresponding gas (0.9 mbar for argon and 1.0 mbar for H_2) before plasma process was necessary to ensure a high purity. The samples were placed in a vertical distance of ~3 cm away from the electrode and surrounded in a Faraday cage with gird to shield any potential bombardment from energetic ions in the plasma. The intensity of the plasma was controlled by tuning the power and pressure of the corresponding gas. The optimal parameters for controlled defect introduction are 20 W/0.9 mbar for Ar and 10 W/1.0 mbar for H_2, respectively. For different experiments explained in the text, different irradiation durations ranging from 30 s to 15 min were used.

Photography

The area of graphene during the experiments was recorded by high resolution photos captured by a Canon Eos 100D photo camera (effective pixels: 18 megapixels, maximum resolution: 5184 × 3456) equipped with a macro lens (Canon EF-S 60mm f/2.8 Macro USM). The camera was positioned perpendicular to the LB trough

(inspected by a sprit level) to minimize the calculation uncertainties. In the optimized condition, deformations as small as few micrometres in each side of the square graphene was detected by this optical set-up.

Image processing

Semi-automatic segmentation of the surface of graphene was performed by means of image registration using *elastix*.[1] Mathematically, the registration problems are formulated as an optimization problem to find the optimum transform parameters that is best solution to map the fixed image domain to the moving image domain. The image at time = 0 was manually segmented and a template was created from this image. The template was the moving image here and all the subsequent images were counted as a fixed image. By registration, the manual segmentation of the first image can be mapped to other images. An affine transform with the cost function of mutual information was used, which was optimized by adaptive stochastic gradient decent over 1500 iterations.

Raman spectroscopy

Raman spectroscopy was performed at the ambient conditions using WITec alpha300 R confocal Raman microscope. The setup was equipped with a dual-axis XY piezo stage providing a minimum step size of 100 nm for sample positioning. Confocal Raman spectroscopy (532 nm excitation wavelength) was used to characterize the graphene samples transferred onto wafers. The laser power was limited to < 2 mW to prevent any laser induced heating of the samples. High resolution spectra were recorded using a 100x Zeiss EC Epiplan-Neofluar DIC objective (NA = 0.9) using 600 lines/mm and 2500 lines/mm spectrometer grating.

AIV. 2 Experimental setup

A commercial available, computer controlled and programmable Langmuir-Blodgett (LB) trough (Minitrough 2, KSV Instruments controlled by KSV Research Lab v2.01 software) was used to perform the compression experiments. Conventionally, the trough has been used to prepare Langmuir films of different molecules and deposit mono- and multilayers onto rigid substrates. Different components of the set-up are marked in Figure AIV.1. The trough has the dimensions of 320 mm × 75 mm × 10 mm. A micro-electronic feedback system controls the surface pressure which is measured based on the Wilhelmy principle, using a platinum plate connected to a sensitive balance. In a typical experiment, the trough was filled with 0.5 M solution of ammonium persulfate (APS) in water. The surface of the air-water interface was aspirated to minimize any contamination, indicated by the surface pressure < 0.2

mN/m after full compression. A piece of graphene sample on copper foil (~1 cm × 1 cm) was placed on surface of APS solution, surrounded with 1,2-dipalmitoyl-*sn*-glycero-3-phosphocholine (DPPC) molecules after dropwisely depositing 1 g/L solution of DPPC lipids (Avanti Polar Lipids Inc.) in $CHCl_3/CH_3OH$ (3:1 volumetric ratio) at the air/water interface with a precision needle mounted on a glass syringe. To prevent large movements of the sample during the copper etching and later, a cage composed of a few wires (with the diameter of few hundreds of micrometres) was implanted in and sticking-out of the Teflon block at the bottom of the trough. A high resolution camera is focused perpendicularly on the sample to record its deformation during the experiments.

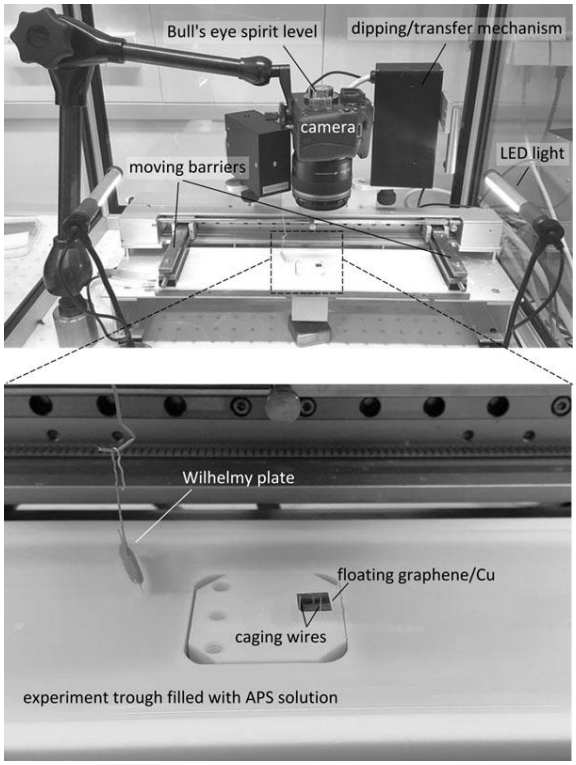

Figure AIV. 1 Experimental setup. The Langmuir–Blodgett trough customized and used for the experiments in this report: different components are marked on the photos.

The copper foil was etched away in ~ 30 minutes yielding graphene floating at the air-water interface. A slight increase of the surface pressure (≤ 1*m*N/m) was observed after the copper etching. Next, two parallel hydrophilic barriers made of Delrin, slightly immersed in the liquid subphase, were moved towards each other. Depending on the specific test, the barrier displacement rates ranged from ~1 mm/min to 12

mm/min. The Wilhelmy plate, positioned close to the center of the trough, was used to measure the surface pressure. The plate was oriented parallel to the barriers. The LB trough was mounted on an anti-vibration table to limit the effect of external vibrations. The experiments were performed under ambient conditions (21℃ < T < 23℃) and humidity level.

AIV. 3 Size-dependent in-plane elastic properties of graphene

Monte Carlo simulations demonstrated that the elastic properties of graphene in the presence of anharmonic coupling the in-plane and out-of-plane displacements are highly size dependent.[2] Particularly the equilibrium bulk modulus of graphene vanishes with the graphene size as $L^{-0.323}$ following the relation:

$$k = \frac{193.6 - 9.1 \times 10^{-2} L^2 + \frac{457.6 \left(\frac{L}{14.14}\right)^4}{L^{0.325}}}{1 + \left(\frac{L}{14.14}\right)^4} \qquad (1)$$

Here L is the length (in Å) and k is the bulk modulus (in N/m) of graphene sample. Bottom inset Figure 1-c superimposes the theoretical and experimental results. Obviously, the size dependency of k can largely explain the considerably low (with respect to earlier reports[1, 3]) in-plane stiffness measured in this work. The median k of our samples, however is slightly above the theory expectation. The suppression of the anharmonicity due to the defects in CVD graphene (as reported previously[3b]) may account for this discrepancy.

AIV. 4 Graphene buckling: blistering or wrinkling

In the process of buckling, thin films delaminate from the surface of *rigid* substrates and form blisters. Similar scenario may happen on the surface of liquids provided that the film/substrate adhesion is small enough; Otherwise the liquid substrate may deform together with the film to form wrinkles. More precisely, the competition between the work of a hydrostatic pressure of the liquid (following the deformation of the film) and surface energy cost to delaminate the film (assuming that the film remains wet after the delamination) determines which buckling mechanism is in action. Wagner et al studied the compression driven bulking of an elastic film floating on a liquid surface;[4] They introduced a dimensionless parameter Γ/δ^2 ($\Gamma \equiv \gamma\lambda/D$ and $\delta \equiv \rho_s t/\rho_l L$, the parameters are explained in Table AIV.1) which sets the critical blister size at the unset of the blistering. Particularly for $\Gamma/\delta^2 >> 1$ (our case), their model

predicts a blistering size of ~ 10 cm, larger than the sample size implying that blistering is impractical for our samples.

Table AIV. 1: parameters involved in calculating the critical blister size, based on the model proposed by Ref (5)

L [m]	1×10^{-2}	initial length of the sample
t [m]	3×10^{-10}	thickness of graphene
ρ_l [kg/m^3]	1×10^{3}	density of water
ρ_s [kg/m^3]	2.2×10^{3}	density of graphene
D [N m]	1×10^{-12}	flexural rigidity of graphene
g [m/t^2]	9.8	gravity acceleration
γ [N/m]	7.3×10^{-2}	surface tension of water
λ [m]	1×10^{-4}	intrinsic wavelength of wrinkles = $(D/\rho_l g)^{1/4}$

AIV. 5 Molecular dynamics simulations

The dynamical response of a monolayer graphene subject to compression was stimulated by means of large scale atomic/molecular massively parallel simulator (LAMMPS).[5] Adaptive intermolecular reactive empirical bond order (AIREBO) potential[6] was chosen to describe interatomic interactions between C-C and C-H pairs. Water molecules have been modelled by the four-point TIP4P potential[7] with the H-O bond length of 0.9572 Å and the H-O-H bond angle of 104.52°. The interaction between atoms accounts for both Coulomb and Van der Waals contributions. To describe the latter, a 6-12 Lennard-Jones (LJ) potential was employed, $4\varepsilon_{ij}\left[\left(\sigma_{ij}/r\right)^{12} - \left(\sigma_{ij}/r\right)^{6}\right]$, with parameters ε_{OO} = 0.1627 kcal/mol and σ_{OO} = 3.1643 Å. The long-range electrostatic interactions were calculated using the particle-particle particle-mesh (PPPM) method. Van der Waals interactions between water molecules and hydrogenated graphene films were characterized by LJ parameters ε_{CO} = 0.0927 kcal/mol and σ_{CO} = 3.2830 Å,[8] and ε_{OH} = 0.0749 kcal/mol and σ_{OH} = 2.9071 Å, where the latter two parameters were obtained from the Lorentz-Berthelot combining rules.

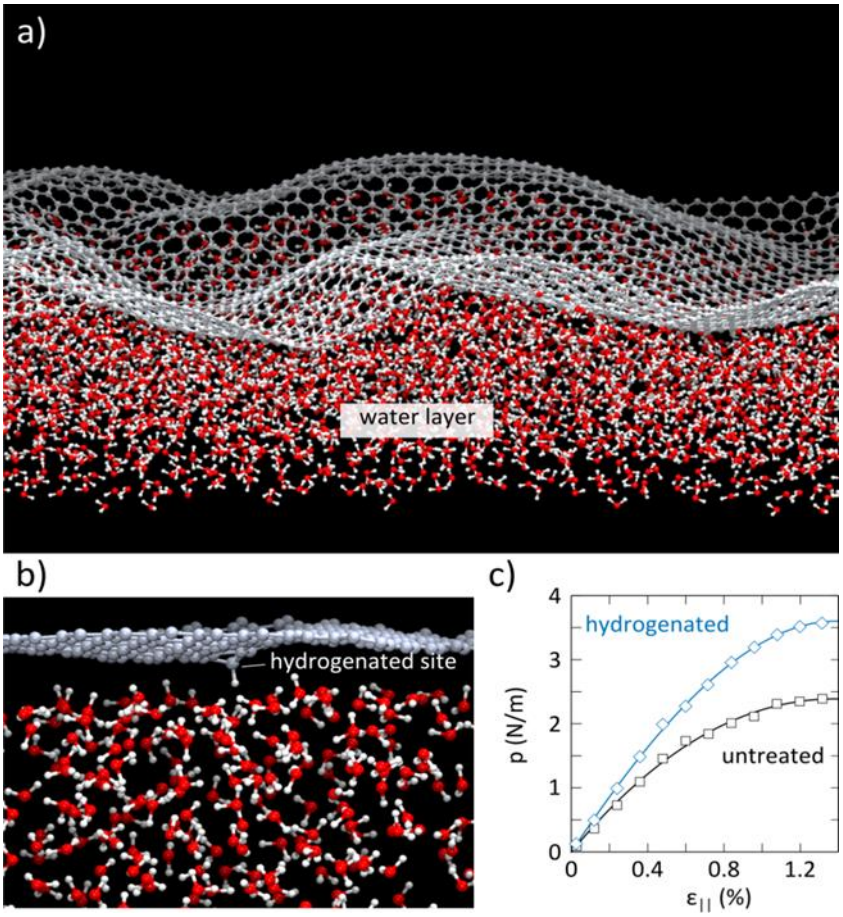

Figure AIV. 2 Molecular dynamics simulation of graphene/water interplay. a) Heavily wrinkled graphene on the surface of water: water molecules follow the undulations of graphene and no delamination is observable. The snapshot corresponds to $\varepsilon > \varepsilon_{cr}$ region. b) Hydrogenated graphene on the surface of water: interaction between the hydrogenated site and water molecules locally stabilizes the corresponding carbon atom. The snapshot corresponds to $\varepsilon < \varepsilon_{cr}$ region. c) Evolution of the stress-stain diagram as a result of the hydrogenation: hydrogenation improves the young's modulus by 1.35 times. The concentration of hydrogenated sites (10^{12} cm^{-2}) in the simulations is similar to the experimentally measured values.

The modeled untreated graphene consist of 3936 carbon atoms spanning roughly square area of 10×10 nm^2. Addition of a single hydrogen atom to this model provides a hydrogen density of 10^{12} cm^{-2}, corresponding to the experimentally measured density for hydrogenated graphene. A relatively thick layer of water molecules with height h_w = 16.7 Å encloses the bottom subspace, from which the lowest water molecules have been kept rigid. Periodic boundary conditions were imposed along the two orthogonal directions parallel to the graphene. Initial equilibration run was

performed under isobaric and isothermal conditions (at room temperature and zero pressure) for 10 ps. The compression process starts by applying a homogeneous biaxial strain with constant rate 0.04 %ps^{-1} within NVT simulations. In all our molecular dynamics simulations, a time step of 1 fs has been used for the velocity-Verlet integrator.

In agreement with the analytical results (see section AIV. 4), the molecular dynamics simulations confirm the absence of blistering in our system (Figure AIV. 2a). Indeed the water molecules follow the undulations of graphene throughout the compression process and no delamination is detectable. Hydrogenation of graphene, on the other hand, locally stabilizes the sheet around the hydrogenated site, implying locally stronger interaction with underlying water molecules (Figure AIV. 2b). The interaction significantly affects the stiffness of graphene (Figure AIV. 2c), resulting in higher bulk modulus than for graphene by a factor of 1.35.

AIV. 6 Flexural rigidity of graphene

Flexural rigidity of graphene governs the onset of buckling. Particularly with Euler's buckling formulation, the critical strain of an square sample reads:

$$\varepsilon_{|cr} = \frac{\pi^2 D}{a^2 E_{2D}} \left(m + \frac{1}{m}\right)^2 \quad (2)$$

Here a is the length (= width), D is the flexural rigidity, E_{2D} is the two-dimensional Young's modulus and m is the number of half waves created upon buckling of the sample. Accordingly the fitting $\varepsilon_{|cr} = \frac{\alpha}{(E_{2D}/\beta)}$ (α = 0.027 N/m, β = 1 for untreated samples) in Figure 1d reveals D:

$$D = \frac{\alpha a^2}{\pi^2 \left(m + \frac{1}{m}\right)^2} \quad (3)$$

The graphene sample strained up to the onset of buckling ($\varepsilon \sim \varepsilon_{cr}$) features numerous horizontal and vertical undulations, separated in $\lambda/2 \sim 50$ μm range providing an estimation for m: $m = a/(\lambda/2) \sim 200$. Accordingly the equation above suggests D in the order of 10^{-12} N m (10^6 eV). This value is six orders of magnitude higher than that for graphene as-grown on Cu(111) recently probed by helium atom scattering (HAS),[9] which can be mainly ascribed to the higher levels of out-of-plane undulations of strain-free graphene floating on water compared to the heavily strained graphene on copper substrate.[10] Moreover, the sizes of the graphene samples (1 cm^2 vs 1 mm^2) can also contribute to the difference in bending rigidity as the undulations magnitudes

increase with the size of graphene. In consequence, high levels of undulations lead to the increased thickness of graphene and thus its bending rigidity.

Numerous half waves observed in our sample is due to the interaction of the graphene with liquid substrate which stabilizes the sheet at high energy levels. Notably in the absence of water, graphene samples would form only one large buckle (m = 1). In this case equation (2) with our estimated flexural rigidity predicts a critical buckling force of 10^{-10} N order which is the same order of the weight of our graphene piece. In other words vertically standing graphene walls would be highly unstable and may collapse by its own weight.

AIV. 7 Strain distribution in crumpled graphene

In details, the deformed graphene was transferred onto an oxidized silicon wafer after being compressed up to 60 mN m^{-1}. Figure AIV. 3a-d present optical micrograph, atomic force microscopy (AFM) and Raman 2D peak position mappings of a selected window of the transferred graphene sample to characterize the strain distribution following the conformation of the wrinkles in crumpled graphene. As shown in Figure AIV 3, the strain field is inhomogeneous and strain is largely concentrated at heavily crumpled wrinkles where the 2D peak is upshifted. The flat areas, in contrast, exhibit a negligible strain as the 2D peak position averages to ~2675 cm^{-1}, an standard value for unstrained graphene.[11] A careful examination of the strain distribution highlights the complex role of the morphology of deformations. Surprisingly, the straight wrinkles (some marked by ☆ in Figure AIV. 3b-c) exhibit negligible contrast with the nearby graphene (background) in the Raman mapping. Those wrinkles are wide enough to be probed by Raman as even narrower but curly wrinkles (such as the one marked by □ in Figure AIV. 3c) are captured with the optics. Gauss's Theorema Egregium assertion expresses the correlation between the morphology and the strain surfaces.[12] The assertion states that straight wrinkles with a single Gaussian curvature identical to flat graphene can exist without any strain. In contrast, for wrinkles with double (multiple) curvatures which are always strained. As unfolding such deformations demands the application of a tensile force, the strain is locked into the heavily crumpled regions (and spreads on neighboring regions) in graphene. The same postulation explains the observed upshift in the 2D peak position along the transition from the marginal (dominant uniaxial compression, featuring straight wrinkles) to the central (biaxial compression with heavily crumpled wrinkles) zones, when the zones are distinguishable (Figure AIV. 3e).

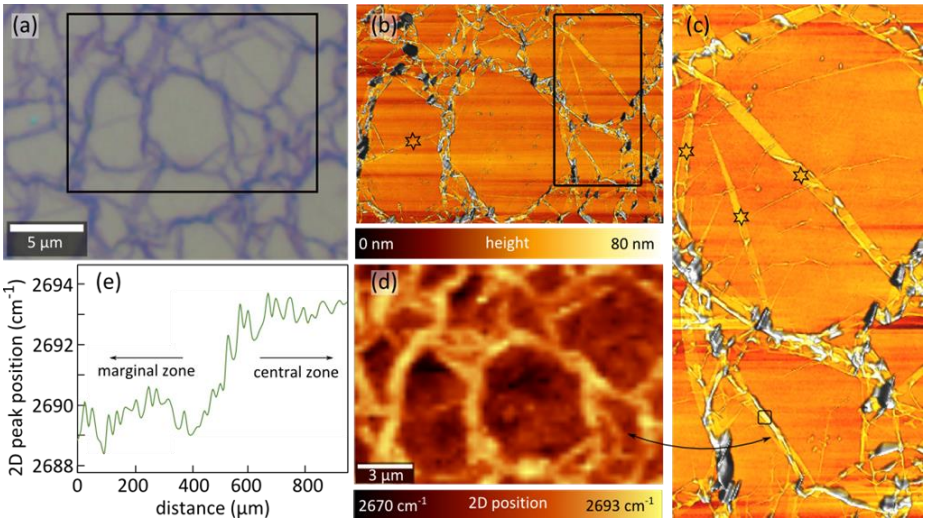

Figure AIV. 3 Strain distribution in crumpled graphene samples. a) Optical micrograph featuring a network of heavily crumpled ridges in graphene. b) AFM mapping of the rectangular window marked in a). c) Zoomed-in AFM mapping of the rectangular window marked in b). d) Two-dimensional map of the position of the Raman 2D peak of graphene, corresponding to the same area in b). e) Line map of the position of the Raman 2D peak of graphene. The low magnification optics (5x) used in this mapping averages the signal over the spot size of ~5.5µm.

AIV. 8 References

[1] A. Zandiatashbar, G.-H. Lee, S. J. An, S. Lee, N. Mathew, M. Terrones, T. Hayashi, C. R. Picu, J. Hone, N. Koratkar, *Nat. Commun.* **2014**, 5, 3186.

[2] J. Los, A. Fasolino, M. Katsnelson, *Phys. Rev. Lett.* **2016**, 116, 015901.

[3] a) C. Lee, X. Wei, J. W. Kysar, J. Hone, *science* **2008**, 321, 385; b) G. López-Polín, C. Gómez-Navarro, V. Parente, F. Guinea, Mikhail I. Katsnelson, F. Pérez-Murano, J. Gómez-Herrero, *Nat. Phys.* **2014**, 11, 26.

[4] T. J. W. Wagner, D. Vella, *Phys. Rev. Lett.* **2011**, 107, 044301.

[5] S. Plimpton, *J. Comput. Phys.* **1995**, 117, 1.

[6] S. J. Stuart, A. B. Tutein, J. A. Harrison, *J. Chem. Phys.* **2000**, 112, 6472.

[7] J. L. F. Abascal, C. Vega, *J. Chem. Phys.* **2005**, 123, 234505.

[8] a) R. R. Nair, H. A. Wu, P. N. Jayaram, I. V. Grigorieva, A. K. Geim, *Science* **2012**, 335, 442; b) P. Hirunsit, P. B. Balbuena, *J. Phys. Chem. C* **2007**, 111, 1709.

[9] A. Al Taleb, H. K. Yu, G. Anemone, D. Farías, A. M. Wodtke, *Carbon* **2015**, 95, 731.

[10] L. A. Belyaeva, L. Jiang, A. Soleimani, J. Methorst, H. J. Risselada, G. F. Schneider, *Liquids relax and unify strain in graphene*, *Nat. Commun.* **2020**, manuscript in press.

[11] G. Tsoukleri, J. Parthenios, K. Papagelis, R. Jalil, A. C. Ferrari, A. K. Geim, K. S. Novoselov, C. Galiotis, *Small* **2009**, 5, 2397.

[12] T. A. Witten, *Rev. Mod. Phys.* **2007**, 79, 643.

Appendix V

Supporting Information for Chapter 6

AV.1 Materials and Methods

Plasma condition

A capacitively coupled plasma system with a radio-frequency (RF) of 40 kHz and a base pressure below 0.02 mbar (Diener electronic, Femto) was employed at room temperature. The power/pressure parameters used for controlled surface modifications were 10 W/1.0 mbar for hydrogen plasma and 16 W/0.85 mbar for ammonia plasma, respectively. Inside the plasma chamber, a perforated Faraday cage was used to shield energetic hydrogen ions to form mild radical plasmas to chemically functionalize the graphene.

Raman characterization

Raman spectroscopy and mapping were collected from CVD graphene on SiO_2/Si substrate (transferred via the PMMA assisted method). The Raman spectrometer used is a WITEC alpha300 R – Confocal Raman Imaging with a laser wavelength of 532 nm. To minimize the potential damage from laser heating effect, the laser power was controlled under 1.1 mW. All of the measurements were performed under ambient conditions at room temperature.

Gas detection experiment

A gastight epoxy chip carriers was used to support the GFET devices, which were placed in a Teflon flow cell. A poly-(dimethylsiloxane) (PDMS) ring was employed to tightly seal the cell. Under the control of mass-flow controllers (MFCs), ethylene, carbon monoxide and ethanol gas (1% in synthetic air) were further diluted with synthetic air (79% N_2 and 21% O_2) to reach different concentrations.

Lock-in technique

A lock-in amplifier (HF2LI, Zurich Instruments) was used to measure the signals with very narrow bandpass filters (~1 Hz). A sinusoidal alternating voltage with an of amplitude of ~10 mV was applied to the GFETs via the source and drain electrodes. The changes of GFETs resistance versus time were monitored using the ZiControl (Zurich Instruments) program. Prior to each measurement, a noise frequency sweep was performed to determine the testing frequencies with minimum noise power spectrum density and thus to optimize the signal-to-noise ratio.

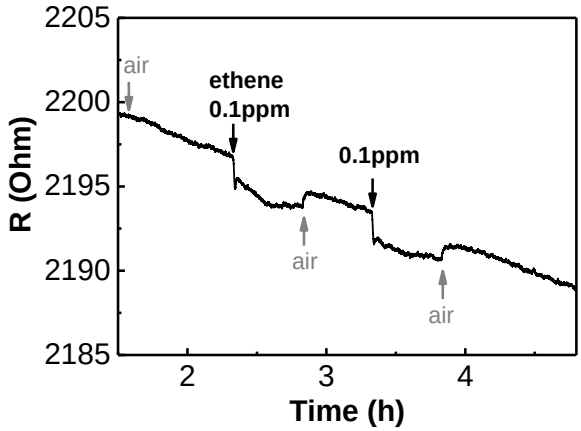

Figure AV. 1 The raw signal from a GFET device upon 0.1 ppm ethylene detection. The sheet resistance exhibits a drifted baseline upon the air exposure. A sharp spike appears due to the initial introduction of 0.1 ppm ethylene, followed by a drop in the signal that stabilizes at a new baseline. Air flush again brings the baseline back to the initial one. A repetitive exposure to ethylene and air gives reproducible results. All the measurements were done at room temperature.